remote sensing

MDPI

Article

Orbit Determination and Positioning for Multi-Objective Mars Exploration Mission Using Same-Beam VLBI Tracking

Yaowei Shi [1], Zhen Zhong [1,*], Xuwei Zhang [2], Shuodong Sun [2], Jianguo Yan [3] and Jean-Pierre Barriot [3]

[1] School of Physics and Electronic Science, Guizhou Normal University, Guiyang 550025, China
[2] Shanghai Aerospace Control Technology Institute, Shanghai 201109, China
[3] State Key Laboratory of Information Engineering in Surveying, Mapping and Remote Sensing, Wuhan University, Wuhan 430079, China
* Correspondence: zzhong@gznu.edu.cn

Highlights

What are the main findings?

- Integrating same-beam VLBI with range-rate observations reduces orbiter 3D position errors by 7.3–33.9%.
- The joint observation strategy achieves a lander positioning accuracy of 33.3 m over a 45-day tracking arc and yields a preliminary estimate of the Martian tidal Love number k_2.

What are the implications of the main finding?

- Same-beam VLBI complements range-rate measurements and improves the precision of Mars orbiter trajectory determination.
- The multi-arc results demonstrate tens-of-meters positioning accuracy for a Martian surface target and identify the sensitivity and limitations of k_2 estimation under the current observation configuration.

Abstract

Precise Mars orbiter orbit determination, high-precision lander positioning and planetary interior parameter inversion are core technical requirements for future Mars exploration. The Tianwen-3 Mars sample-return mission requires coordinated orbiter–lander operations, imposing stricter demands on deep-space radio measurements. The Martian tidal Love number k_2 describes Mars' interior structure and tidal response; its accurate estimation constrains the core-mantle configuration and thermal evolution. This study is a simulation-based observability analysis rather than an empirical determination of the Martian tidal parameters. It establishes a joint framework for orbit determination, lander positioning and tidal parameter estimation by integrating ground range-rate and orbiter–lander same-beam VLBI (Very Long Baseline Interferometry) observations. The high-fidelity dynamical models are adopted to build observation models, accounting for the Martian gravity field with degree and order 120, third-body perturbations, solar radiation pressure, relativistic effects and solid tides. Weighted batch least-squares is used to jointly estimate orbiter states, lander coordinates and k_2, and the influence of observation arc length on solution accuracy is analyzed. Simulation residuals match preset noise levels. Adding VLBI data reduces the orbiter's 3D position error by 7.3–33.9%, with an average reduction of approximately 16.8% and full-arc error below 1.6 m. Longer arcs improve lander positioning, reducing 3D error from 88.418 m (7-day) to 33.349 m (45-day). The retrieved k_2 0.152866 ± 0.0487 agrees with the reference value of 0.152. However, the current two-station same-beam setup and arc length yield weak empirical constraints on k_2, requiring longer observation spans or improved geometries to recover the Martian tidal parameters from real data. Same-beam

Check for updates

Academic Editor: Jose Moreno

Received: 8 October 2026
Revised: 6 November 2026
Accepted: 9 November 2026
Published: 13 November 2026

Copyright: © 2026 by the authors. Licensee MDPI, Basel, Switzerland. This article is an open access article distributed under the terms and conditions of the Creative Commons Attribution (CC BY) license.

VLBI provides complementary geometric constraints unavailable from range-rate alone, supporting multi-spacecraft orbit solutions and Martian interior inversion for Tianwen-3.

Keywords: Mars; same-beam VLBI; differential phase delay; precise orbit determination

1. Introduction

With the continuous development of deep-space exploration technology, planetary missions are evolving from single-spacecraft exploration toward more complex mission architectures involving coordinated orbiters, landers, and other spacecraft [1–3]. As an important terrestrial planet in the Solar System, Mars has become a major target for planetary science research and deep-space exploration [4,5]. In such multi-target missions, high-precision spacecraft orbit determination and target positioning are essential for reliable mission operations and effective utilization of scientific observations. Compared with near-Earth missions, Mars exploration involves long communication distances, significant signal delays, complex dynamical environments, and limited ground tracking and control resources. In particular, the relative geometry between an orbiter and a surface lander must be accurately determined to support communication, navigation, and coordinated operations [6].

Traditional deep-space radio tracking techniques primarily rely on radiometric observables such as range and range-rate measurements for spacecraft orbit determination [7,8]. Range observations directly provide constraints on the radial distance between the spacecraft and ground tracking stations, whereas range-rate observations provide line-of-sight velocity information through frequency-shift measurements. However, the availability of deep-space tracking and control resources is limited, which becomes particularly important for future Mars exploration missions involving multiple targets, such as an orbiter and a lander. Same-beam VLBI (Very Long Baseline Interferometry) observations can serve as a complementary measurement technique by exploiting the existing high-precision tracking of the orbiter to provide differential information for lander positioning, thereby reducing the need for additional dedicated tracking resources.

VLBI has been widely applied to deep-space exploration and can provide high-precision angular information that complements conventional range and range-rate measurements [9–12]. Compared with conventional measurements, VLBI provides angular constraints that can improve the geometric observability of spacecraft orbit determination [13]. This capability is particularly relevant to Mars landers, which are fixed on the planetary surface and cannot generate additional observation geometry through orbital motion. Same-Beam VLBI utilizes signals from the orbiter and lander entering the antenna beam of the same tracking station simultaneously. Through differential-delay observations, part of the systematic errors can be effectively eliminated, thereby further improving the relative positioning capability between the orbiter and lander [14,15]. Previous studies have investigated VLBI-based orbit determination, observation accuracy, and different tracking modes, including applications to Mars spacecraft and lander positioning [9,16,17]. Studies of Mars exploration have also demonstrated the potential of combining VLBI with conventional radiometric observations for spacecraft orbit determination and lander positioning. Nevertheless, systematic analyses of the complementary contributions of different observation types to the joint orbit determination of a Mars orbiter and the positioning of a surface lander remain limited, particularly when the correlations between spacecraft states, lander position, and dynamical parameters are considered simultaneously.

This issue is particularly relevant to future multi-spacecraft Mars exploration missions such as Tianwen-3, which involves coordinated operations among an orbiter, lander, and

ascent vehicle. In addition to spacecraft and target positioning, high-precision radio tracking data can support planetary radio science by constraining dynamical parameters of Mars. The tidal Love number k_2 is an important parameter describing the tidal response of Mars and is related to its interior structure [18]. Its estimation can be affected by spacecraft orbital errors, the adopted Martian gravity field model, observation geometry, and correlations among estimated parameters. Consequently, the observation configuration used for multi-target orbit determination may affect not only spacecraft and lander positioning but also the estimation of Martian dynamical parameters.

Therefore, this study develops a joint orbit determination and positioning framework for a Mars orbiter–lander configuration based on the Tianwen-3 mission scenario. The framework incorporates a high-fidelity dynamical model including the Martian non-spherical gravity field, solar and planetary perturbations, solar radiation pressure, and relativistic corrections. Based on the Small Body and planets Precise Orbit Determination Toolkit (SPOT, Python v3.9) developed by Wuhan University, ground-based range-rate observations and orbiter–lander same-beam VLBI observations are jointly processed using a weighted least-squares approach. The initial state of the orbiter, the lander position, and selected dynamical parameters are estimated simultaneously. The effects of different observation combinations and observation durations are evaluated in terms of orbiter orbit errors, lander positioning errors, observation residuals, parameter estimation biases, and formal errors. The results provide a quantitative assessment of the potential of same-beam VLBI to complement conventional deep-space radiometric tracking for multi-target Mars exploration and planetary radio science.

2. Model Construction and Parameter Estimation

2.1. Dynamic Models

When a Mars orbiter operates in the vicinity of Mars, its orbital state is governed not only by the central gravitational attraction of Mars but also jointly affected by various perturbing forces, including the non-spherical gravity field of Mars, gravitational perturbations from the Sun and other celestial bodies, solar radiation pressure, relativistic effects, and tidal deformation of Mars. For precise orbit determination, although some perturbations are relatively small compared with the central gravitational acceleration of Mars, they can produce cumulative effects over long observation arcs and may become coupled with the orbital state parameters, thereby affecting the final orbit determination accuracy and the estimation results of dynamical parameters.

In this study, the major perturbing forces involved in the orbiter's motion are comprehensively modeled according to the actual dynamical environment of Mars exploration missions. The specific configuration of the dynamical parameters is presented in Table 1.

The total acceleration experienced by the orbiter can be expressed as

$$a = a_{gv} + a_{pm} + a_{srp} + a_{rel} + a_{tide} \quad (1)$$

where a_{gv} is the acceleration induced by the non-spherical gravitational field of Mars, a_{pm} is the point-mass third-body gravitational perturbation, a_{srp} is the solar radiation pressure acceleration, a_{rel} is the relativistic correction acceleration, and a_{tide} is the additional acceleration generated by the solid tides of Mars.

For a Mars orbiter operating in the vicinity of the planet, the gravitational attraction of Mars is the dominant dynamical factor governing the orbital motion. Because the actual mass distribution of Mars is not strictly spherically symmetric, a central point-mass model alone cannot adequately represent the true gravitational environment experienced by the orbiter. Therefore, the spherical harmonic gravitational model of Mars is adopted to compute the non-spherical gravitational acceleration.

Table 1. Configuration of simulation parameters for Mars orbiter and beam observation.

Dynamical Model Parameters	Description	Value/Configuration
Mars gravitational field	The MRO120D model [19]	Degree/order 120; normalized spherical-harmonic coefficients
N-body perturbation	The major celestial bodies within the solar system: Sun, Mercury, Venus, Earth, Jupiter, Saturn, Uranus, Neptune, Pluto. Using the DE440 ephemeris.	Ephemerides DE440 (planets) and MAR099 (Mars satellites)
	Mars' Satellites: Phobos and Deimos using the MAR099 ephemeris.	
Solar radiation pressure model	Cannonball model	$C_R = 1.5$; $A = 15\ \mathrm{m}^2$; $m = 2000$ kg; $A/m = 7.5 \times 10^{-3}\ \mathrm{m}^2/\mathrm{kg}$
Relativistic effect	Including the Schwarzschild term	Applied for Sun, Mercury, Venus, Earth, Mars, Jupiter
Mars solid tide	Degree-2 Love-number model	Tidal Love Number: $k_2 = 0.152$ [20]; tide-raising bodies: Sun and Earth
Numerical integrator	DOP853 (8th-order Runge–Kutta), adaptive step	Relative Tolerance = Absolute Tolerance = 1×10^{-11}; observation sampling interval 60 s

The gravitational potential of Mars can be expressed as

$$V(r,\phi,\lambda) = \frac{\mu_M}{r}\left[1 + \sum_{n=2}^{N}\left(\frac{R_M}{r}\right)^n \sum_{m=0}^{n} \overline{P}_{\mathrm{nm}}(\sin\phi)\left(\overline{C}_{nm}\cos m\lambda + \overline{S}_{nm}\sin m\lambda\right)\right] \quad (2)$$

where μ_{M} is the gravitational parameter of Mars, R_{M} is the reference radius of Mars, r is the distance from the orbiter to the center of mass of Mars, ϕ and λ denote the areographic latitude and longitude of the orbiter, respectively, $\overline{P}_{\mathrm{nm}}$ is the fully normalized associated Legendre function, $\overline{C}_{\mathrm{nm}}$ and $\overline{S}_{\mathrm{nm}}$ are the spherical harmonic coefficients of the Martian gravitational field, and N is the maximum degree and order of the gravitational field. The gravity field model adopted in this study is MRO120D with degree and order of 120 [19].

In addition to the gravitational attraction of Mars itself, the orbiter is also subject to gravitational perturbations from the Sun and other solar system bodies, which are described by point-mass models in this study. Solar radiation pressure is one of the main non-conservative forces acting on the spacecraft. Although the solar radiation pressure acceleration is far smaller than the gravitational acceleration of Mars, its long-term cumulative effect can induce systematic deviations in the orbital state. Therefore, the Cannonball solar radiation pressure model is adopted, and the corresponding acceleration can be expressed as

$$a_{srp} = P_0 C_R \frac{A}{m}\left(\frac{r_0}{r}\right)^2 \hat{s} \quad (3)$$

where P_0 is the solar radiation pressure at the reference distance from the Sun, C_{R} is the solar radiation pressure coefficient, A is the effective illuminated area of the spacecraft, m is the spacecraft mass, and r is the distance between the orbiter and the Sun.

Relativistic effects were also taken into account in the spacecraft dynamics model to further improve the accuracy of orbit determination. The relativistic corrections are described by the first-order post-Newtonian Schwarzschild term, which accounts for the

relativistic effects arising from the gravitational fields of major solar system bodies. The corresponding acceleration can be expressed as

$$a_{rel} = \left(\frac{GM}{c^2 r^3}\right)\left[\left(\frac{4GM}{r} - v^2\right)\mathbf{r} + 4(\mathbf{r}\cdot\mathbf{v})\mathbf{v}\right] \quad (4)$$

where GM is its gravitational parameter, c is the speed of light in vacuum, $\mathbf{r}$ is the position vector directed from the perturbing body to the orbiter and $r = |\mathbf{r}|$ is its magnitude, $\mathbf{v}$ is the velocity vector of the orbiter relative to the perturbing body and $v = |\mathbf{v}|$ is its magnitude, and $\mathbf{r}\cdot\mathbf{v}$ denotes the scalar product of $\mathbf{r}$ and $\mathbf{v}$. The total relativistic perturbation is obtained by summing this acceleration over the Sun and the selected planets.

In addition to the dynamical factors described above, the influence of Martian solid tides on the orbiter's motion is further considered. When Mars is subject to the gravitational attraction of external bodies such as the Sun and its satellites, periodic tidal deformation occurs in the interior of the planet, inducing small temporal variations in the Martian gravitational field. For precise orbit determination, the time-varying gravitational field generated by solid tides is reflected in the radio observables through the orbiter's motion; therefore, high-precision radio tracking data can be used to invert the tidal response parameters of Mars. In this study, the second-degree tidal Love number k_2 is adopted to describe the response of Mars to the external tidal potential, and the tidal effects generated primarily by the Sun and the Earth are considered. The corresponding tidal perturbation acceleration can be expressed as

$$a_{tide} = \nabla U_{tide} = \nabla k_2 \left(\frac{R_M}{r}\right)^3 W_2 \quad (5)$$

where U_{tide} is the additional tidal gravitational potential of Mars, whose magnitude and spatial distribution depend on the radius of Mars, the positions of the external perturbing bodies, and the second-degree Love number k_2. A reference value of $k_2 = 0.152$ is adopted for the Martian tidal parameter and is subsequently treated as one of the estimated parameters [20]. In this way, the sensitivity of different radio observables to the Martian tidal parameter can be further analyzed, thereby extending the conventional orbit determination problem to the radio inversion of the Martian interior structure parameters.

Combining the dynamical factors described above, a comprehensive dynamical model for the Mars orbiter is constructed, with the non-spherical gravitational attraction of Mars as the dominant term, supplemented by third-body perturbations and solar radiation pressure, and further incorporating relativistic corrections and Martian solid tides. The spacecraft parameters, including the orbiter mass, the effective illuminated area, and the solar radiation pressure coefficient, are configured according to the simulated mission conditions, and the Martian tidal Love number is initialized with its reference value. The orbit is propagated using the high-order DOP853 Runge–Kutta numerical integration method, from which the position and velocity states of the orbiter over the entire simulated arc are obtained for a given initial state and dynamical model. The resulting orbital states are used, on the one hand, to construct the range-rate observation geometry between the ground tracking stations and the orbiter, and, on the other hand, to establish the relative geometric relationship between the orbiter and the lander on the Martian surface, from which the same-beam VLBI observables are further computed. The dynamical model thus provides a unified state-propagation basis for orbiter orbit determination, lander positioning, and the estimation of the Martian tidal Love number k_2 under the joint range-rate and same-beam VLBI observation scheme.

2.2. Observation Model Construction

Based on the SPOT platform [21], a simulation model for the same-beam VLBI observations between the Mars orbiter and the lander is established, and orbiter orbit determination,

lander positioning, and Martian tidal parameter estimation are investigated within a unified dynamical and observation modeling framework. To illustrate the same-beam VLBI observation geometry, the observation structure of the Mars orbiter–lander configuration is shown in Figure 1.

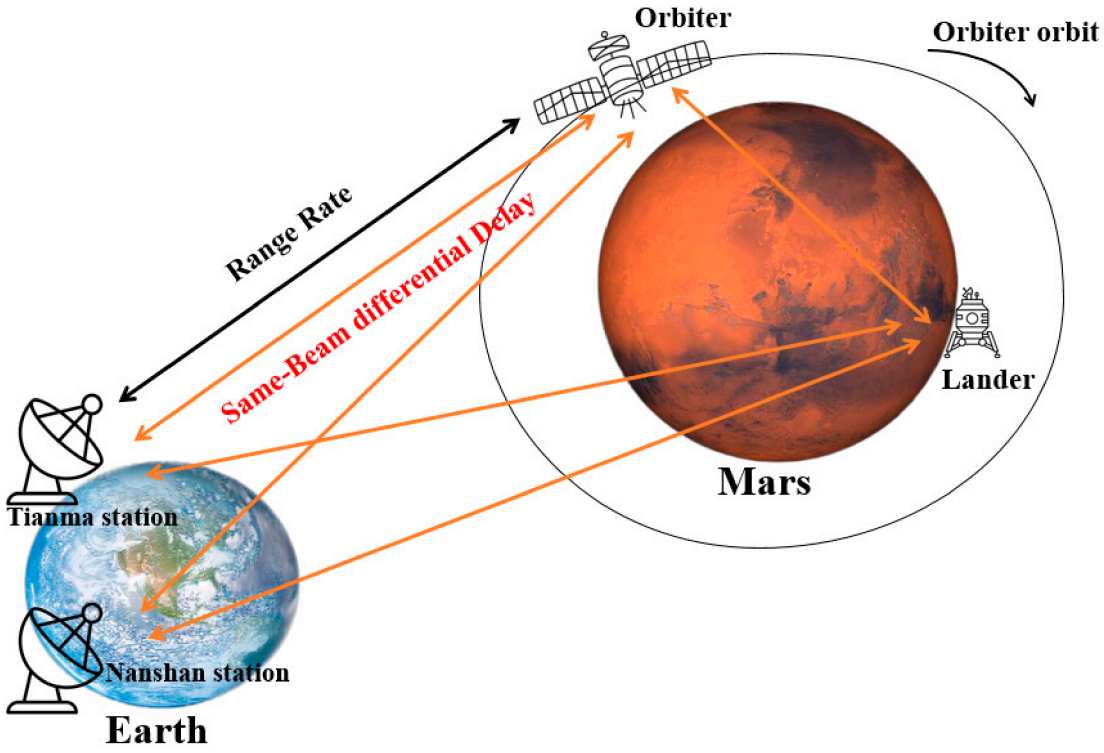


Figure 1. Observation diagram of the Mars orbiter–lander configuration. The VLBI stations in Shanghai and Xinjiang, China, are considered in this study. Their approximate locations are (31.2°N, 121.4°E) and (43.8°N, 87.6°E), respectively. The corresponding parameters of the orbiter and lander are described in the following sections.

Same-beam VLBI exploits the condition that the signals of the orbiter and the lander enter the antenna beams of both ground stations simultaneously. Let r_o and r_l denote the position vectors of the orbiter and the lander, R_A and R_B those of the Tianma and Nanshan stations, and c the speed of light. The same-beam VLBI can then be expressed as

$$\tau(t_r) = \frac{1}{c} \cdot \{[\|r_l - R_B\| - \|r_o - R_B\|] - [\|r_l - R_A\| - \|r_o - R_A\|]\} \quad (6)$$

where the spacecraft position vectors are evaluated at the emission epochs and the station position vectors at the reception epoch t_r. The first bracket gives the range difference between the lander and the orbiter as seen from station B, and the second bracket gives the corresponding inter-spacecraft range difference as seen from station A. This double-differenced observable is mainly sensitive to the relative angular geometry of the two spacecraft and exhibits low sensitivity to their absolute ranges. For this reason, same-beam VLBI measurements can complement station-to-orbiter range-rate observations.

The emission epoch of each signal is obtained by fixed-point iteration. Starting from $t^{(0)}\{s,k\} = t_r$, the emission epoch of the signal from spacecraft k ($k = o, l$) to station s ($s = A, B$) is updated as

$$t^{(i+1)}\{s,k\} = t_r - \|r_k(t^{(i)}\{s,k\}) - R_s(t_r)\|/c \quad (7)$$

until the change in the computed range falls below 1×10^{-8} km (≈0.01 mm) or a maximum of ten iterations is reached.

The one-way range also includes the Shapiro delay caused by the solar gravitational field,

$$\Delta\rho\{s,k\} = -\left(2GM_{\odot}/C^2\right) \cdot \ln[(r_s + r_k + \rho\{s,k\})/(r_s + r_k - \rho\{s,k\})] \quad (8)$$

where $r_{\mathrm{s}} = \|R_{\mathrm{s}} - \mathrm{r}_{\square}\|$ and $r_{\mathrm{k}} = \|r_{\mathrm{k}} - \mathrm{r}_{\square}\|$ are the heliocentric distances of the station and the spacecraft, so that the range entering Equation (6) is $\rho\{s,k\} + \Delta\rho\{s,k\}$. In the observation model, this Shapiro term is the only relativistic correction retained: the second-order Doppler shift and light aberration are below the 0.1 mm/s and 0.1 ns noise levels adopted here and are therefore not modelled.

The observable measured in practice is the differential phase delay, which is determined modulo the observing wavelength and is therefore ambiguous, but considerably more precise than the differential group delay obtained from the phase slope across the synthesised bandwidth. In real same-beam VLBI, the group delay is used to resolve the integer phase ambiguity, after which the phase delay provides the high-precision observable [11,12]. The observable generated in this simulation is the geometric differential delay of Equation (6), i.e., the value that the differential phase delay would take once the ambiguity has been resolved; it therefore corresponds to the phase-delay observable rather than to the group-delay observable.

No phase-wrapping is simulated: the observable is generated directly in its unwrapped form, which corresponds to the case in which the phase ambiguity has been fully resolved. A residual ambiguity error, if present, would act as a constant bias on the same-beam observable; its magnitude is bounded by the group-delay accuracy, which for the 4 MHz synthesised bandwidth assumed here is at the sub-nanosecond level, and is therefore below the 0.1 ns noise level adopted in the simulation.

The double-differenced observable is intrinsically common-mode rejecting, and the treatment of the individual error sources has been established for the Chinese VLBI network (CVN) same-beam measurements. At a given station, the station clock offset is common to both spacecraft and therefore cancels exactly in the orbiter-minus-lander difference; likewise, the tropospheric and ionospheric delays, the solar plasma delay and the station-dependent instrumental delays are nearly identical for the two spacecraft, which lie inside the same antenna beam and are observed simultaneously, so that only their small residuals survive the differencing [15,17]. The inter-station differencing of the baseline then removes the remaining station-dependent terms. The transponder delay, which differs between the orbiter and the lander and therefore does not cancel, is treated as a constant bias that is calibrated or absorbed into the estimated parameters. Since these common-mode terms have been modelled and experimentally verified for the Chang'e and Tianwen-1 same-beam VLBI data, they are not re-derived here; the simulation instead adopts the observation noise level implied by that error budget.

The same-beam observations are assumed to be carried out in the S/X band with the multi-channel bandwidth-synthesis configuration of the CVN used for the Chang'e and Tianwen-1 missions [2,14]; the synthesised bandwidth and the integration time (60 s) determine the group-delay accuracy used to resolve the phase ambiguity, while the phase delay provides the high-precision observable. The antenna beam width is about 0.1°, which is much larger than the angular separation of the orbiter and the lander, so that both spacecraft are always observed within the same beam when the station is tracking them. A visibility criterion of 5° elevation is applied simultaneously for both spacecraft at both stations; together with the station–orbiter–lander geometry, this criterion limits the effective same-beam window to only a few hours per day.

The assumed 0.1 ns noise corresponds to a differential range error of about 3 cm. This level is consistent with, and on the conservative side of, the differential phase-delay precision reported for same-beam VLBI of Chinese lunar and Mars missions, where the post-fit formal precision of the phase delay reaches the picosecond level [22] and the Tianwen-1

same-beam positioning experiment achieved accuracies at the corresponding scale [23]. The 0.1 ns value therefore represents a realistic, slightly conservative estimate of the achievable random measurement noise rather than an optimistic assumption.

The mission scenario considered in this study consists of the Earth, Mars, a Mars orbiter, a lander on the Martian surface, and ground-based deep-space tracking stations. The ground station-to-orbiter range-rate observation link provides constraints on the orbital state of the orbiter by measuring the radial velocity between the station and the orbiter. Compared with a single station-to-orbiter measurement, the multi-node joint observation configuration formed by two ground stations, the orbiter, and the lander provides more geometric information. Because the same-beam VLBI is sensitive to the relative distance variation between the orbiter and the lander, it can be processed jointly with the ground-station-to-orbiter range-rate observations, thereby improving the observation geometry and enhancing the observability of the orbital and dynamical parameters.

2.3. Parameter Estimation Method

The initial state of the orbiter x_o, the position of the lander x_l, and the dynamical parameters including the Martian tidal Love number k_2 and the solar radiation pressure coefficient C_R are treated as estimated parameters and jointly estimated using a weighted batch least-squares method. The observation equation is expressed as

$$z = h(x) + \varepsilon \tag{9}$$

where z is the observation vector, $h(x)$ is the observation model, and ε is the observation noise. The least-squares estimation minimizes the weighted sum of squared residuals

$$J(x) = (z - h(x))^T W (z - h(x)) \tag{10}$$

to obtain the optimal estimates of the estimated parameters, and the iterative correction is given by

$$\Delta\dot{x} = \left(H^T W H\right)^{-1} H^T W (z - h(x)) \tag{11}$$

where $H = \partial h / \partial x$ is the Jacobian matrix of the observation model with respect to the estimated parameters and W is the observation weight matrix. Upon iterative convergence, the joint estimation results of the orbiter state, the lander position, and the Martian tidal parameters are obtained.

3. Results

3.1. Orbiter Orbit Determination Simulation Analysis

To validate the effectiveness of the established Mars orbiter–lander joint observation model and the parameter estimation method, parameter estimation is first performed on simulated observation data. The initial orbital elements of the orbiter adopted in the orbit determination simulation are listed in Table 2, with the initial epoch set to 00:00:00.00 1 January 2030.

Table 2. Configuration of the initial orbital elements of the orbiter.

	Semi-Major Axis (km)	**Eccentricity**	**Inclination (°)**	**RAAN (°)**	**Argument of Periapsis (°)**	**Mean Anomaly (°)**
orbiter	3790.0	0.010	30	40	20	9.8

To simulate the Martian surface exploration scenario, the lander is placed in a candidate landing area in Utopia Planitia with areographic coordinates of 107°E and 17°N, and the mean radius of Mars is taken as 3389.5 km. The ground-based same-beam VLBI observations

involve two tracking stations, Shanghai Tianma Station and Xinjiang Nanshan Station. During the simulation, Range-rate observations from the Kashi Station and orbiter–lander same-beam VLBI observations on the Tianma–Nanshan baseline are used, with noise levels of 0.1 mm/s for the range-rate observations and 0.1 ns for the same-beam VLBI observations, and a sampling interval of 60 s for both. Considering the actual observation geometry, the differential-delay observations are constrained by the station–orbiter–lander geometry and visibility conditions, so that their effective observation windows are markedly shorter than those of the range-rate observations. Consequently, the subsequent parameter estimation results are obtained under limited same-beam VLBI observation windows, which is closer to the situation encountered in real deep-space radio observations affected by observation geometry and visibility.

The orbital dynamical differential equations are integrated numerically to generate a near-circular orbit with an altitude of 360–420 km, which serves as the reference orbit for the subsequent observation simulation and parameter estimation. To examine the influence of initial orbital errors on parameter estimation, artificial initial errors are introduced on the basis of the reference orbital state, with a deviation of 100 m imposed on each of the three position components of the orbiter, thereby constructing a parameter estimation scenario with certain initial errors. The initial state errors are substantially amplified in the computation of the observation model, leading to a high initial normalized residual cost, which reflects the significant deviation between the initial estimated parameters and the reference truth values as well as the pronounced discrepancy between the model-predicted observables and the simulated observations. After iterative least-squares estimation, the cost function decreases continuously, indicating that the parameter estimation method can effectively correct the initial state deviations and progressively reduce the discrepancy between the model-computed and simulated observations. To further examine the fitting performance and convergence behavior of the observation model before and after parameter estimation, Figure 2 presents the variation in the range-rate residuals.

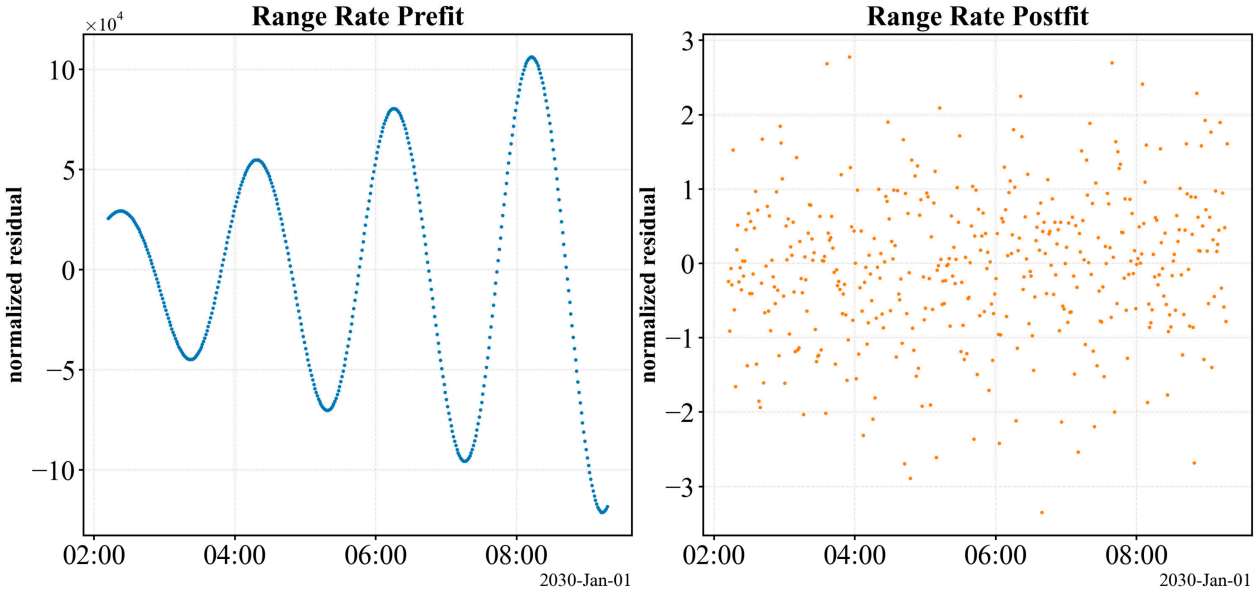


Figure 2. Comparison of normalized residuals before and after parameter estimation for speed measurement observations. The (**left**) sub-image shows the Prefit normalized residuals before parameter estimation, while the (**right**) sub-image shows the Postfit normalized residuals after the least-squares iteration. The weighted mean of the residuals after fitting is $W_{mean} = -0.051$, and the weighted root mean square is $W_{RMS} = 0.978$. This arc segment is taken from 1 January 2030.

As shown in Figure 2, the normalized range-rate residuals before parameter estimation exhibit large magnitudes and pronounced periodic oscillations with time, reaching the order of 10^4, indicating significant deviations between the initial orbital state and the state predicted by the dynamical model, as well as systematic discrepancies between the model-computed and simulated observations. After least-squares parameter estimation, the normalized range-rate residual magnitudes decrease substantially, with the vast majority of the residuals concentrated within the interval of −3 to 3 and fluctuating randomly around zero. The post-fit residuals show no evident systematic offsets or persistent trends within the individual observation arcs, indicating that the estimated orbital state parameters fit the range-rate observations well. Since the WRMS (Weighted Root Mean Square) is close to unity, the post-fit residual level is consistent with the prescribed observation noise level. In summary, the results in Figure 2 demonstrate that the range-rate observations can effectively constrain the orbital state and substantially correct the initial orbital state deviations, thereby validating the effectiveness of the parameter estimation method. Figure 3 presents the residual behavior of the same-beam VLBI observations.

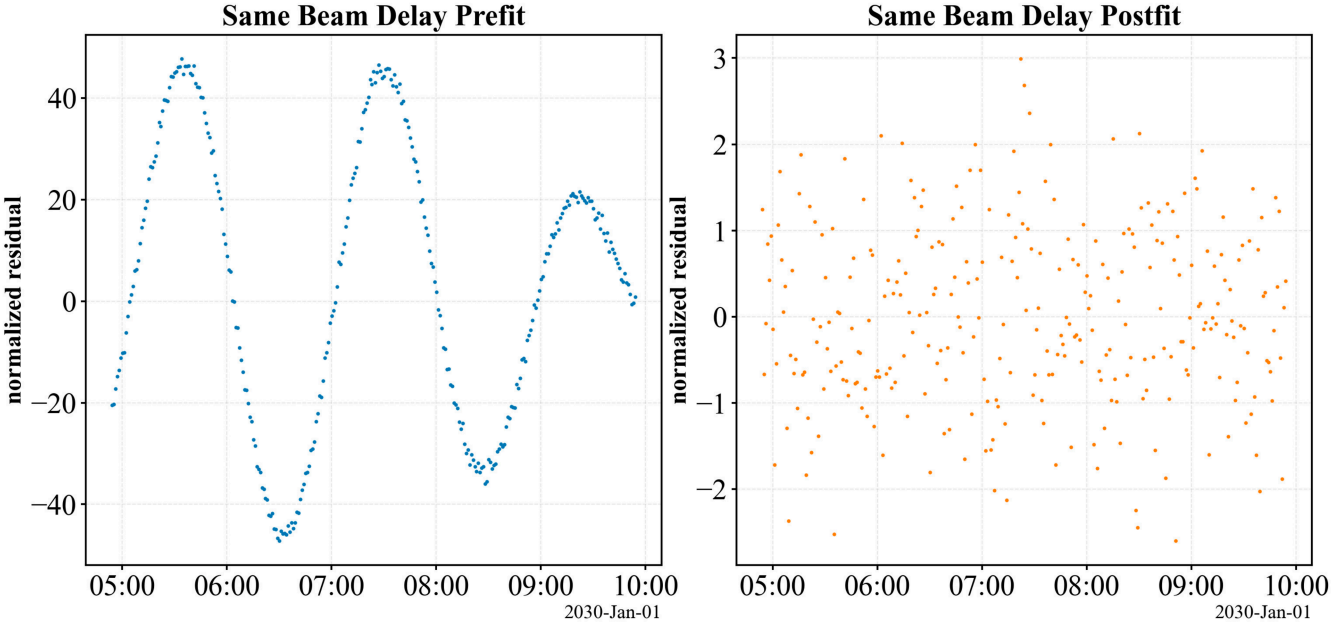


Figure 3. Comparison of normalized residuals before and after parameter estimation of observation values in beam-based VLBI measurements. The (**left**) sub-image shows the Prefit normalized residuals before parameter estimation, while the (**right**) sub-image shows the Postfit normalized residuals after the least-squares iteration. The weighted mean of the residuals after fitting is $W_{mean} = 0.004$, and the weighted root mean square is $W_{RMS} = 1.040$. This arc segment is taken from 1 January 2030.

As shown in Figure 3, the pre-fit normalized residuals of the same-beam VLBI observations exhibit pronounced periodic oscillations with magnitudes up to approximately ±50, reflecting that the initial state deviations of the orbiter and the lander introduce systematic periodic errors into the differential-delay observation model and that obvious discrepancies exist between the theoretically computed delays and the simulated observations. After the orbiter–lander joint parameter estimation, the post-fit residuals of the same-beam VLBI are substantially attenuated, with the vast majority of the residual samples falling within the interval of −3 to 3 and distributed randomly around zero. The post-fit residual sequence exhibits no significant long-period trends or fixed inter-arc offsets, indicating that the joint estimation effectively suppresses the delay-observation biases induced by the coupling of the initial state errors of the orbiter and the lander. The post-fit W_{RMS} being close to unity indicates that the residual fluctuation level is essentially consistent with the prescribed

observation noise. These results validate the compatibility between the established same-beam VLBI observation model and the orbital dynamical model, and demonstrate that the same-beam VLBI observations can impose strong constraints on the relative geometric configuration between the orbiter and the lander, providing reliable observational support for lander positioning and the inversion of related dynamical parameters.

From the residual convergence results in Figures 2 and 3, the range-rate and same-beam VLBI observations exhibit good complementarity in parameter estimation. The range-rate observables are sensitive to the absolute orbital state of the orbiter and can effectively constrain its absolute orbital evolution, whereas the same-beam VLBI observables directly constrain the relative geometric configuration between the orbiter and the lander and can reduce the influence of common-mode orbit errors. On the basis of the validated observation-model fitting performance, the estimated orbiter position errors obtained from the iteration are further examined to quantitatively assess the recovery accuracy of the absolute orbital state. Table 3 presents the three-dimensional orbiter position estimation errors for the two schemes, namely the range-rate-only solution and the joint solution. Table 4 provides details of the arc segments considered in Table 3.

Table 3. The three-dimensional position error of the arc segments of the orbiter. The X/Y/Z error represents the difference between the estimated initial orbital position components and the reference position components in the J2000 inertial coordinate system. The 3D total position error is calculated by $\sqrt{X^2 + Y^2 + Z^2}$. Reduction (%) = (Position Error with Range-Rate Only − Position Error with Range-Rate and SBI (Same-Beam Interferometry))/Position Error with Range-Rate Only × 100.

Observation Arc	X Error (m)	Y Error (m)	Z Error (m)	Position Error with Range-Rate Only (m)	Position Error with Range-Rate and SBI (m)	Reduction (%)
Arc 1	0.068	−0.159	0.398	0.507	0.433	14.6
Arc 2	−0.351	−0.119	−0.685	0.840	0.779	7.3
Arc 3	0.043	−0.069	0.161	0.249	0.181	27.3
Arc 4	0.108	−0.166	0.560	0.641	0.594	7.3
Arc 5	0.144	−0.483	1.461	1.712	1.546	9.7
Arc 6	−0.041	−0.281	0.536	0.919	0.607	33.9

Table 4. Arc Segment Definition Explanation.

Observation Arc	Start (UTC)	End (UTC)	Duration	Same-Beam Window (UTC)
Arc 1	01-01-2030 00:00:00	01-01-2030 23:59:59	1 day	04:54–09:54
Arc 2	02-01-2030 00:00:00	02-01-2030 23:59:59	1 day	04:52–09:54
Arc 3	03-01-2030 00:00:00	03-01-2030 23:59:59	1 day	04:50–09:55
Arc 4	05-01-2030 00:00:00	05-01-2030 23:59:59	1 day	04:46–09:56
Arc 5	11-01-2030 00:00:00	11-01-2030 23:59:59	1 day	05:42–09:59
Arc 6	15-01-2030 00:00:00	15-01-2030 23:59:59	1 day	08:27–10:01

The reference trajectory is obtained by a single numerical integration over 15 days (1–15 January 2030), and the single-arc simulations are then initialized from the states of this common 15-day reference orbit, so that all arcs share exactly the same dynamical model and differ only in their initial epochs. Each arc spans one full UTC (Coordinated Universal Time) day (00:00:00–23:59:59), which corresponds to one rotation of Mars (24.6 h) and one diurnal cycle of the Earth, so that the complete diurnal variation in the observation geometry is contained within a single arc. Six of the fifteen daily arcs are retained for the orbit-validation analysis: the first three consecutive days (1–3 January) and three further days (5, 11 and 15 January) distributed over the remaining part of the 15-day span. This selection keeps the number of single-arc solutions manageable, avoids the nearly redundant

geometry of adjacent days, and at the same time samples the evolution of the same-beam visibility conditions from the beginning to the end of the 15-day reference orbit.

As shown in Table 3, compared with the range-rate-only solution, the three-dimensional position errors of all arcs decrease to varying degrees after the same-beam VLBI observations are introduced, indicating that the same-beam VLBI observations can further enhance the observability of the orbital state on the basis of conventional range-rate observations. The degree of improvement varies among the arcs, suggesting that the constraining capability of the same-beam VLBI observations depends not only on the observation noise level but also on the observation geometry and the variation in the orbital state within each arc. For the range-rate-only solutions, the three-dimensional position errors of the individual arcs range from 0.249 to 1.712 m; after joint estimation with same-beam VLBI observations yields reduced three-dimensional position errors for all six arcs. The magnitude of this relative improvement varies markedly between arcs, spanning 7.3% (Arcs 2 and 4) to 33.9% (Arc 6), with a mean per-arc improvement of approximately 16.8%. This 7.3–33.9% range reflects the scatter of individual arc improvements and does not denote an overall improvement. These discrepancies across arcs are related to the observation geometry and the variation in the orbital state within each arc. This demonstrates that the same-beam VLBI introduces transverse geometric information, which is difficult to obtain from range-rate observations alone, through the orbiter–lander differential path, effectively compensating for the insufficient constraints of range-rate-only observations in the direction perpendicular to the line of sight and yielding positive gains for the orbital state estimation of all arcs. In terms of the individual components, the Z-direction position deviations of all arcs are larger than the X- and Y-direction deviations, which is consistent with the feature that the normal component exhibits the largest error amplitude in the RTN (Radial–Along-track–Normal) analysis shown in Figure 4, reflecting that the joint observations impose relatively weaker geometric constraints on the out-of-plane and vertical components. In each coordinate direction, the deviations of each arc segment include both positive and negative values, and there is no continuous one-way systematic offset, indicating that the estimation results are not dominated by a persistent systematic deviation. Overall, the joint solution controls the three-dimensional orbiter position errors of all arcs within 1.6 m, achieving high-precision estimation of the absolute orbital state of the orbiter.

From the time series of the orbiter position estimation errors in the RTN frame shown in Figure 4, it can be seen that, after parameter estimation converges, the radial, along-track, and normal components all exhibit pronounced periodic variations, with different amplitudes and offsets among the three directions. Unlike the observation residuals, which primarily characterize the consistency between the fitted and observed measurements, the RTN position errors directly describe the evolution of the estimated orbital state over the observation arc. The three components exhibit a common periodicity consistent with the orbital motion, indicating that the observed fluctuations are closely related to the orbital dynamics and the time-varying observation geometry rather than purely random measurement noise.

The radial error exhibits stable periodic oscillations, with values ranging from approximately −0.1 to 1.25 m. Although the error is not symmetrically distributed around zero, its oscillation envelope remains bounded throughout the observation arc without a persistent unidirectional accumulation or divergence trend. The relatively stable behavior of the radial component indicates that the radial orbital state is effectively constrained under the joint observation scheme.

The along-track error also exhibits periodic variations with the same characteristic period as the other two components, ranging approximately from −0.72 to 0.76 m. It has the smallest overall variation amplitude among the three components and remains approxi-

mately centered around zero throughout the observation arc. No evident unidirectional accumulation or divergence is observed, indicating that the along-track state remains stable after parameter estimation.

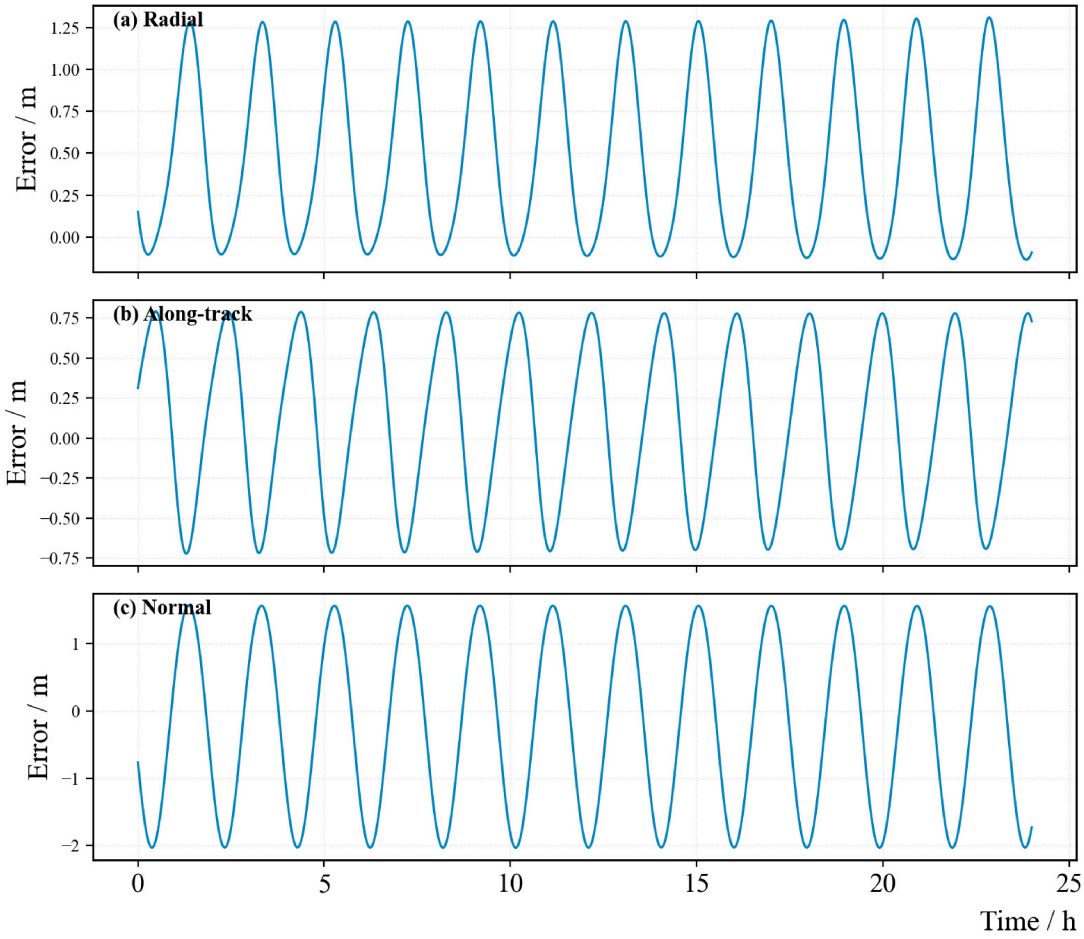


Figure 4. Orbiter position errors in RTN frame. (**a**) Radial component; (**b**) Tangential component; (**c**) Normal component; The abscissa represents the observation time, and the ordinate represents the position estimation error. The periodic fluctuations of the steady-state error are caused by the periodic changes in the observation geometry with the orbital motion.

The normal-direction error exhibits the largest variation amplitude among the three components, ranging approximately from −2.0 to 1.5 m. Despite its relatively large amplitude, the oscillation envelope remains stable throughout the observation arc, with no evident secular growth or divergence. Since the normal direction represents out-of-plane motion, the bounded behavior of this component indicates that the orbital-plane state is also stably maintained over the observation arc.

The range-rate observables are primarily sensitive to velocity variations along the line of sight between the orbiter and the ground station, whereas the same-beam VLBI observations provide complementary geometric constraints through the differential path between the orbiter and the lander. The two types of observations therefore provide complementary constraints on the orbital state, particularly for transverse components that are relatively difficult to constrain using range-rate observations alone. Overall, the RTN position errors remain at the meter level without evident divergence throughout the observation arc. The common periodicity observed in the three components, together with their different amplitudes and offsets, reflects the combined effects of orbital dynamics and the time-varying observation geometry rather than purely random measurement noise. Therefore, the RTN

time-series analysis not only demonstrates the stable evolution of the estimated orbital state under the joint observation scheme, but also provides an important complement to the observation-residual analysis by revealing the error characteristics at the orbital-state level.

3.2. Multi-Arc Lander Positioning Analysis

Unlike the orbiter, the lander is fixed on the Martian surface in the simulation, and its position parameters and the tidal Love number k_2 are treated as global parameters and jointly estimated over multiple arcs using the same-beam VLBI observations. To investigate the influence of the observation arc length on the estimation of the lander position parameters, observation arcs of 7, 15, 30, and 45 days are selected for the joint solutions, and the lander positioning accuracy under different arc lengths is compared and analyzed. The parameter estimation results are presented in Table 5.

Table 5. The landing vehicle positioning error obtained through the joint orbit determination of multiple segments. The X/Y/Z errors represent the differences between the estimated and reference lander coordinates in the Mars body-fixed frame. They are obtained from the joint orbit determination using multiple orbital segments. The 3D total position error is calculated by $\sqrt{X^2 + Y^2 + Z^2}$.

Observation Arc	X Error (m)	Y Error (m)	Z Error (m)	Number of Same-Beam VLBI Observations	Total 3D Position Error (m)
7-day arc	−37.271	−7.200	−79.854	2156	88.418
15-day arc	−45.151	49.903	−33.259	3974	75.067
30-day arc	28.045	−8.934	26.087	9053	39.331
45-day arc	−33.213	−3.009	−0.041	15,736	33.349

As shown in Table 5, the three-dimensional lander positioning error decreases continuously with increasing observation arc length, from approximately 100 m for the 7-day arc to 33.349 m for the 45-day arc. The convergence, however, is direction-dependent. For short arcs, the Z-direction error dominates because the limited variation in observation geometry results in unbalanced observability among the position components. As the arc length increases, the errors become more evenly distributed among the three coordinate directions, indicating that the multi-arc observations provide increasingly diverse geometric constraints and improve the separability of the estimated position parameters. The improvement also becomes less pronounced for longer arcs, suggesting that the information gain from newly added observations gradually approaches saturation under the adopted two-station same-beam configuration. To further investigate the directional behavior of the positioning errors, the sensitivity of the same-beam VLBI to the three lander position components is analyzed in the Mars body-fixed frame and is presented in Figure 5.

As shown in Figure 5, the RMS sensitivities to the X, Y, and Z components are 26.9, 18.9, and 10.8 ps/km, respectively, indicating that the Z-direction is the least sensitive to the same-beam VLBI observations. This relatively weak instantaneous sensitivity makes the Z-component more difficult to constrain over a short observation arc. However, the positioning accuracy is determined not only by the instantaneous sensitivity but also by the variation in the observation geometry over time. As the observation arc increases, the Earth's diurnal rotation and the changing Earth–Mars geometry lead to different baseline orientations in the Mars body-fixed frame, providing complementary constraints on the lander position. These additional geometric constraints progressively improve the observability of the initially weakly constrained Z-direction, resulting in its pronounced convergence over the longer observation arcs.

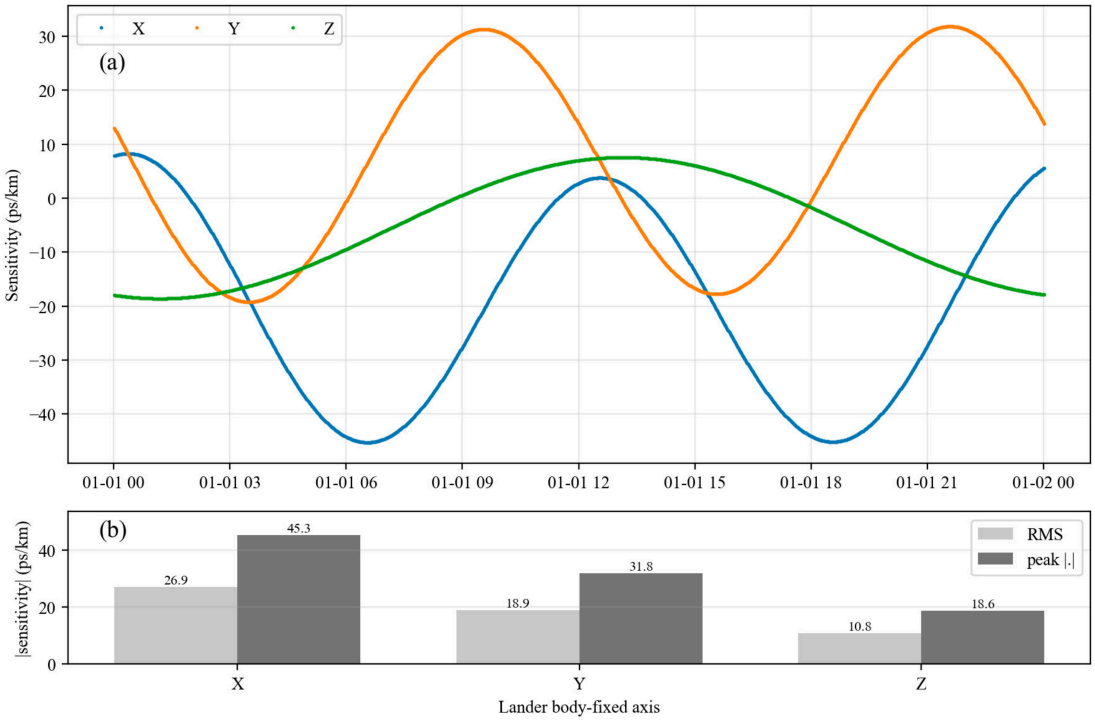


Figure 5. Sensitivity of the same-beam VLBI to the lander position components in the Mars body-fixed frame. (**a**) Time series of the sensitivity components; (**b**) RMS and peak sensitivities in the X, Y, and Z directions.

3.3. Analysis of the Martian Tidal Love Number k_2 Estimation

The Martian tidal Love number k_2 characterizes the response of Mars to external tidal forcing and is closely related to the physical properties of its interior, making it an important parameter for investigating the Martian interior structure. In this study, k_2 is treated as a global parameter and jointly estimated with the orbiter state and lander position using multi-arc range-rate and same-beam VLBI observations. For the 45 single-day arcs, the estimated value is 0.152866 ± 0.0487, corresponding to an absolute deviation of 0.0009 and a relative deviation of approximately 0.6% from the reference value of 0.152. The estimate converges to the vicinity of the reference value, indicating that, under the current dynamical model and observation accuracy conditions, the radio tracking data contain identifiable Martian tidal response signals. However, the formal constraint on k_2 over this arc remains weak, and the reliable estimation of the tidal parameter awaits the accumulation of signals over longer observation arcs.

To check that the estimator is not biased towards the reference value, a Monte Carlo retrieval test was carried out with two representative true values of k_2, 0.152 and 0.169, using independent single-arc realizations, The results are presented in Table 6. The recovered means are 0.1534 and 0.1697, with biases of only +0.0014 and +0.0007, meaning that the estimator returns the true value without systematic bias and within the formal uncertainty of about 0.050. Arcs whose same-beam geometry yields a formal uncertainty above 0.3, and which therefore provide no meaningful constraint on k_2, were excluded from the statistics.

Table 6. Monte Carlo retrieval of k_2.

True k_2	Number of Realizations	Recovered k_2	Bias	Formal
0.152	50	0.1534	0.0014	0.0502
0.169	50	0.1697	0.0007	0.0497

4. Discussion

4.1. Comparison with Previous Studies and Interpretation

These results are consistent with, but also extend, previous studies on Martian surface-target positioning. Yang et al. [22] investigated Tianwen-1 rover positioning using same-beam VLBI observations between the orbiter and rover and showed that the rover positioning accuracy strongly depends on the accuracy of the orbiter orbit. With approximately 6 h of same-beam VLBI observations, improving the orbiter orbit accuracy from the kilometer level to the hundred-meter level or better enabled rover positioning at the level of several hundred meters. Tong et al. [23] further demonstrated the high measurement sensitivity of in-beam source-frequency phase-referenced VLBI using actual Zhurong rover observations, with the formal precision of the post-fit phase delay reaching the picosecond level (approximately 1.3 ps). The corresponding 1σ formal precision of the three-dimensional VLBI positioning solution was approximately $\pm 0.06'$ in longitude, $\pm 0.22'$ in latitude, and ± 219.5 m in height, indicating a formal positioning precision at the level of several hundred meters. However, differences at the kilometer level remained between the VLBI-derived positions and those from the Tianwen-1 GNC (Guidance, Navigation, and Control) and visual localization systems. The authors attributed this discrepancy mainly to the kilometer-level orbit error of the Tianwen-1 orbiter, which was used as the reference calibrator. This result highlights that high-precision relative VLBI measurements do not directly translate into equivalent absolute positioning accuracy.

Unlike these studies, the present work jointly estimates the orbiter state and lander position within a unified multi-arc orbit determination framework rather than assuming a fixed or known orbiter orbit. The long-term same-beam VLBI observations therefore contribute directly to the joint estimation of the orbiter–lander relative geometry. The reduction of the three-dimensional positioning error to 33.349 m over 45 days demonstrates that extending the observation arc can substantially strengthen the absolute positioning constraints while partially mitigating the propagation of orbiter orbit errors into the lander position. These results highlight the combined importance of high-precision relative observations, accurate orbiter orbit determination, and long-term multi-arc estimation for improving the absolute positioning of Martian surface targets.

4.2. Sources of Uncertainty and Limitations

The estimated value is also comparable in magnitude with previous determinations. Yoder et al. [24] obtained $k_2 = 0.153 \pm 0.017$ from Mars Pathfinder range-rate tracking data, while Konopliv et al. [19] derived $k_2 = 0.1697 \pm 0.0027$ from multi-year Mars Reconnaissance Orbiter tracking data. The estimated value of 0.152866 obtained in this study lies within the interval spanned by the above observed values and theoretical predictions, and is particularly close to the Mars Pathfinder result, which corroborates the reasonableness of the k_2 estimation results under the joint orbit determination and positioning framework. It should be noted that the simulation arc length in this study does not exceed 45 days, which is far shorter than the multi-year tracking arcs of MRO; therefore, the differences between the estimated value and the literature values mainly arise from the reference value setting and the arc length limitation, and cannot be directly equated with the tidal parameter inversion accuracy in real missions. To further investigate the source of the weak formal constraint on k_2, the parameter correlation matrix of a representative single-arc solution is shown in Figure 6.

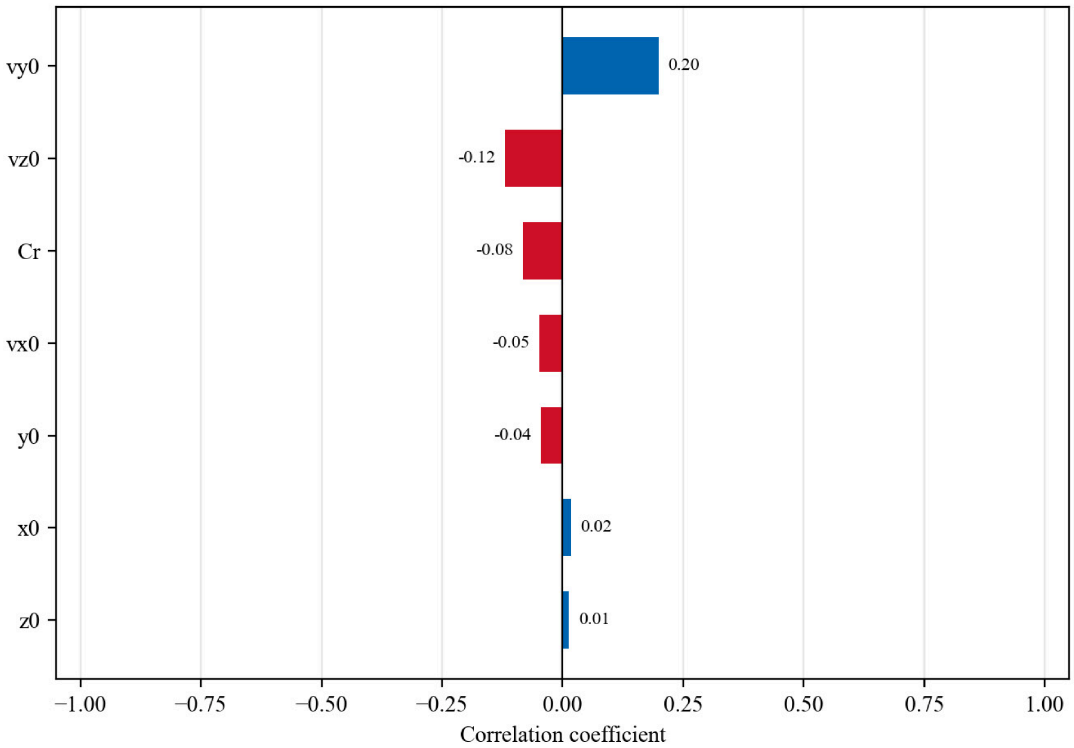


Figure 6. The correlation coefficient between the Mars tidal Love number k_2 and the estimated parameters. Red indicates negative correlations, while blue indicates positive correlations. k_2 is most strongly correlated with the velocity components of the orbiter initial state and with the solar radiation pressure coefficient C_R, whereas its correlations with the position components and with the lander coordinates are negligible.

The k_2 a priori constraint is deliberately relaxed so that the resulting correlations primarily reflect the information provided by the observation geometry. The correlations are generally weak but exhibit a clear directional pattern. The largest correlations are found between k_2 and the initial velocity components, with $|\rho| = 0.199$ for $v\mathrm{y}_0$ and $|\rho| = 0.119$ for $v\mathrm{z}_0$, followed by the solar radiation pressure coefficient C_R ($|\rho| = 0.082$). In contrast, the correlations with the initial position components are all below 0.044, while those with the three lander coordinates are below 2×10^{-4}.

The observed correlation structure is physically reasonable because both the tidal Love number and C_R affect the spacecraft trajectory through acceleration perturbations. Over a relatively short observation arc, part of the tidal acceleration signature can therefore be absorbed by adjustments to the initial velocity and C_R. The very small correlations with the lander coordinates, however, indicate that the tidal-parameter estimation does not significantly compete with the lander-position estimation. Since the maximum correlation coefficient is only about 0.2, parameter correlation is unlikely to be the dominant limitation on k_2 in the present configuration. Instead, the relatively weak formal constraint mainly reflects the small magnitude of the tidal perturbation and the limited accumulation of its signature over the 45-day observation span. Extending the observation period would allow the tidal signal to accumulate under changing observation geometries and could consequently improve the separability and formal precision of k_2. Incorporating additional observations and tidal parameters, such as h_2 and l_2, may provide further constraints in future studies.

4.3. Future Research Directions

Future work can be carried out in the following aspects: first, more tracking stations or combined range data can be introduced to break through the geometric bottleneck of the two-station same-beam VLBI observations and further improve the absolute positioning accuracy of the lander; second, the tracking arcs can be extended and the second-degree Love numbers h_2 and l_2 can be jointly estimated to deepen the constraints on the interior structure and tidal response of Mars; third, sensitivity analyses of the observation noise, parameter correlations, and dynamical model errors can be conducted to systematically evaluate the robustness of the joint estimation framework, thereby providing more comprehensive technical support for the implementation of the Tianwen-3 mission.

5. Conclusions

This study focuses on the coordinated orbiter–lander exploration scenario of the Tianwen-3 Mars sample-return mission. Based on the SPOT precise orbit determination software platform, a precise dynamical model incorporating the degree-120 non-spherical gravitational field of Mars, third-body perturbations, solar radiation pressure, relativistic corrections, and Martian solid tide perturbations is established, together with ground-based deep-space station range-rate and orbiter–lander same-beam VLBI observation models. A weighted batch least-squares method is employed to perform multi-arc joint estimation of the orbiter state, lander position, and Martian tidal Love number k_2. The effects of observation arc length on orbit determination, lander positioning, and tidal parameter estimation are systematically investigated.

The simulation results show that the post-fit W_{RMS} residuals of the range-rate and same-beam VLBI observations reach 0.978 and 1.040, respectively, consistent with the prescribed observation noise levels and indicating good consistency between the dynamical and observation models. Compared with the range-rate-only solution, the inclusion of same-beam VLBI observations reduces the three-dimensional orbiter position errors by approximately 7.3–33.9% for individual arcs, corresponding to an average reduction of around 16.8%. In the multi-arc joint solution, the three-dimensional orbiter position errors remain below 1.6 m while the RTN errors remain at the meter level without evident divergence. These results demonstrate the effectiveness of combining range-rate and same-beam VLBI observations for constraining the absolute orbital state of the orbiter.

For lander positioning, the three-dimensional positioning error decreases from 88.418 m to 33.349 m as the observation arc length increases. The 30-day arc contributes the main accuracy improvement, and the 45-day arc further eliminates the residual errors of the vertical components.

The jointly estimated Martian tidal Love number k_2 is 0.152866 ± 0.0487, which is close to the reference value of 0.152 and falls within the range of estimates reported in previous studies. However, the relatively large formal error indicates that the sensitivity to k_2 remains limited under the current observation configuration and arc lengths. Longer observation arcs and improved observation geometry are therefore required to obtain tighter constraints on the Martian tidal response.

Author Contributions: Conceptualization, Y.S., Z.Z., X.Z., S.S., J.Y. and J.-P.B.; Methodology, Y.S., Z.Z., X.Z., S.S., J.Y. and J.-P.B.; Software, Y.S.; Validation, Y.S. and J.Y.; Formal analysis, Y.S.; Investigation, Y.S., X.Z. and S.S.; Resources, J.Y.; Data curation, Y.S.; Writing—original draft, Y.S.; Writing—review & editing, Z.Z., X.Z., S.S., J.Y. and J.-P.B.; Visualization, Y.S. and S.S.; Supervision, Z.Z., X.Z., J.Y. and J.-P.B.; Project administration, Z.Z., J.Y. and J.-P.B.; Funding acquisition, Z.Z. and J.Y. All authors have read and agreed to the published version of the manuscript.

Funding: This work is supported by the National Natural Science Foundation of China (Grant Nos. 42364001 and 42241116) and National Key Research and Development Program of China (No. 2022YFF0503202).

Data Availability Statement: The planetary ephemerides and Mars gravity field models used in this study are obtained from publicly available data sources, as cited in the manuscript. The software SPOT (Python v3.9) employed in this work is available upon request from the corresponding author.

Acknowledgments: The authors would like to thank the PDS project for providing the planetary ephemerides and Mars gravity field models.

Conflicts of Interest: The authors declare no conflicts of interest.

References

1. Zuber, M.T.; Lemoine, F.G.; Smith, D.E.; Konopliv, A.S.; Smrekar, S.E.; Asmar, S.W. Mars Reconnaissance Orbiter Radio Science Gravity Investigation. *J. Geophys. Res. Planets* **2007**, *112*, E05S07. [CrossRef]
2. Yan, J.; Yang, X.; Ye, M.; Li, F.; Jin, S.; Jin, W.; Barriot, J.-P.; Li, H. New Tracking Modes and Performance for Mars Spacecraft Orbit Determination and Lander Positioning. *Planet. Space Sci.* **2018**, *163*, 5–13. [CrossRef]
3. Takeuchi, H.; Yoshikawa, K.; Takei, Y.; Oki, Y.; Kikuchi, S.; Ikeda, H.; Soldini, S.; Ogawa, N.; Mimasu, Y.; Ono, G.; et al. The Deep-Space Multi-Object Orbit Determination System and Its Application to Hayabusa2's Asteroid Proximity Operations. *Astrodynamics* **2020**, *4*, 377–392. Correction in *Astrodynamics* **2022**, *6*, 441–443. https://doi.org/10.1007/s42064-022-0136-2. [CrossRef]
4. Mazarico, E.M.A. Precise Orbit Determination of the Mars Odyssey Spacecraft and Geodetic Inversion for the Martian Gravity Field. Master's Thesis, Massachusetts Institute of Technology, Cambridge, MA, USA, 2004.
5. Ryne, M.; Graat, E.; Haw, R.; Kruizinga, G.; Lau, E.; Martin-Mur, T.; McElrath, T.; Nandi, S.; Portock, B. Orbit Determination for the 2007 Mars Phoenix Lander. In Proceedings of the AIAA/AAS Astrodynamics Specialist Conference, Honolulu, HI, USA, 18–21 August 2008. Paper AIAA 2008-7215. [CrossRef]
6. Yan, J.; Wang, B.; Yang, X.; Ye, M.; Gao, W.; Li, F.; Barriot, J.-P. The Application of Inverse VLBI Measurement in Mars Orientation Parameter Solutions. *Icarus* **2021**, *370*, 114662. [CrossRef]
7. Hong, X.; Zhang, X.; Zheng, W.; Wang, G.; Liu, Q.; Wang, N.; Zhang, H.; Wang, M.; Shu, F. Research Progress of VLBI Technology and Application to China Lunar Exploration Project. *J. Deep Space Explor.* **2020**, *7*, 321–331. [CrossRef]
8. Liu, S.; Yan, J.; Cao, J.; Ye, M.; Li, X.; Li, F.; Barriot, J.-P. Review of the Precise Orbit Determination for Chinese Lunar Exploration Projects. *Earth Space Sci.* **2021**, *8*, e2020EA001361. [CrossRef]
9. Liu, Q.; Wu, Y.; Huang, Y.; Zheng, X.; Li, P. Mars Rover Positioning Technology Based on Same-Beam VLBI. *Sci. China Phys. Mech. Astron.* **2015**, *45*, 099502. [CrossRef]
10. Liu, Q. VLBI Orbit Determination Technology for Mars Exploration. *J. Deep Space Explor.* **2018**, *5*, 435–441. [CrossRef]
11. Zhou, H.; Yan, J.-G.; Xu, D.-Z.; Huang, Y.; Li, H.-T. Method for differential phase delay resolution of phase referencing VLBI technique and its experimental verification. *Res. Astron. Astrophys.* **2021**, *21*, 296. [CrossRef]
12. Zhou, H.; Xu, D.-Z.; Yan, J.-G.; Chen, S.-W.; Li, H.-T. A new method for resolving phase ambiguity in radio interferometry using Earth rotation synthesis. *Res. Astron. Astrophys.* **2021**, *21*, 167. [CrossRef]
13. Fiori, F.; Tortora, P.; Zannoni, M.; Ardito, A.; Menapace, M.; Bellei, G.; Budnik, F.; Morley, T.; Mercolino, M.; Orosei, R. Deep space orbit determination via Delta-DOR using VLBI antennas. *CEAS Space J.* **2022**, *14*, 421–430. [CrossRef]
14. Liu, Q.; Chen, M.; Goossens, S.; Kikuchi, F.; Matsumoto, K.; Ping, J.; Wang, G.; Zheng, W.; Hanada, H.; Hong, X. The application of coaxial beam VLBI in precise orbit and position measurement of multi-target detectors in sampling return mode. *Sci. Sin. Phys. Mech. Astron.* **2010**, *40*, 809–818. [CrossRef]
15. Liu, Q.; Wu, Y. Application of high precision VLBI technology in deep space exploration. *J. Deep Space Explor.* **2015**, *2*, 208–212. [CrossRef]
16. Niu, D.; Duan, J.; Wang, M.; Chen, L.; Lu, W.; Ren, T. A study of the orbit determination ability and time-sharing acquisition mode for China's Deep Space Network VLBI data. *J. Deep Space Explor.* **2021**, *8*, 495–502. [CrossRef]
17. Liu, Q.; Huang, Y.; Shu, F.; Wang, G.; Zhang, J.; Chen, Z.; Li, P.; Ma, M.; Hong, X. VLBI technique for the orbit determination of Tianwen-1. *Sci. Sin. Phys. Mech. Astron.* **2022**, *52*, 239507. [CrossRef]
18. Rivoldini, A.; Van Hoolst, T.; Verhoeven, O.; Mocquet, A.; Dehant, V. Geodesy constraints on the interior structure and composition of Mars. *Icarus* **2011**, *213*, 451–472. [CrossRef]
19. Konopliv, A.S.; Park, R.S.; Folkner, W.M. An improved JPL Mars gravity field and orientation from Mars orbiter and lander tracking data. *Icarus* **2016**, *274*, 253–260. [CrossRef]
20. Konopliv, A.S.; Yoder, C.F.; Standish, E.M.; Yuan, D.-N.; Sjogren, W.L. A global solution for the Mars static and seasonal gravity, Mars orientation, Phobos and Deimos masses, and Mars ephemeris. *Icarus* **2006**, *182*, 23–50. [CrossRef]

21. Yan, J.; Gao, W.; Wang, B.; Sun, S.; Yang, W.; Barriot, J.-P. Small body and planets precise orbit determination toolkit (SPOT) and its application. *Sol. Syst. Res.* **2025**, *59*, 24. [CrossRef]
22. Tong, F.; Zheng, W.; Zhang, J. An in-beam source-frequency phase referencing VLBI positioning method for China's first Martian rover. *Publ. Astron. Soc. Pac.* **2024**, *136*, 024503. [CrossRef]
23. Yang, P.; Huang, Y.; Li, P.; Liu, Q.; Qin, S.; Shan, Q.; Liu, S. Positioning and accuracy analysis of Tianwen-1 Mars rover based on same-beam VLBI measurement. *Geom. Inf. Sci. Wuhan Univ.* **2023**, *48*, 84–91. [CrossRef]
24. Yoder, C.F.; Konopliv, A.S.; Yuan, D.N.; Standish, E.M.; Folkner, W.M. Fluid core size of Mars from detection of the solar tide. *Science* **2003**, *300*, 299–303. [CrossRef] [PubMed]

Disclaimer/Publisher's Note: The statements, opinions and data contained in all publications are solely those of the individual author(s) and contributor(s) and not of MDPI and/or the editor(s). MDPI and/or the editor(s) disclaim responsibility for any injury to people or property resulting from any ideas, methods, instructions or products referred to in the content.